



HAL
open science

Hybrid control of self-oscillating resonant converters

Nicola Zaupa, Luis Martínez-Salamero, Carlos Olalla, Luca Zaccarian

► **To cite this version:**

Nicola Zaupa, Luis Martínez-Salamero, Carlos Olalla, Luca Zaccarian. Hybrid control of self-oscillating resonant converters. *IEEE Transactions on Control Systems Technology*, inPress, Early access, pp.1-8. 10.1109/TCST.2022.3179948 . hal-03614816

HAL Id: hal-03614816

<https://hal.science/hal-03614816>

Submitted on 21 Mar 2022

HAL is a multi-disciplinary open access archive for the deposit and dissemination of scientific research documents, whether they are published or not. The documents may come from teaching and research institutions in France or abroad, or from public or private research centers.

L'archive ouverte pluridisciplinaire **HAL**, est destinée au dépôt et à la diffusion de documents scientifiques de niveau recherche, publiés ou non, émanant des établissements d'enseignement et de recherche français ou étrangers, des laboratoires publics ou privés.

Hybrid control of self-oscillating resonant converters

Nicola Zaupa, Luis Martínez-Salamero, *Senior Member, IEEE*, Carlos Olalla, *Member, IEEE*,
and Luca Zaccarian, *Fellow, IEEE*

Abstract—We describe parallel and series resonant converters via a unified set of input-dependent coordinates whose dynamics is intrinsically hybrid. We then propose a hybrid feedback showing a self-oscillating behavior whose amplitude and frequency can be adjusted by a reference input ranging from zero to π . For any reference value in that range we give a Lyapunov function certifying the existence of a unique nontrivial hybrid limit cycle whose basin of attraction is global except for the origin. Our results are confirmed by experimental results on a series resonant converter prototype.

Index Terms—Lyapunov methods, Stability of hybrid systems, Resonant converters, Power electronics, Power conversion.

I. INTRODUCTION

RESONANT converters are well-known in the power electronics industry due to numerous advantages, including soft-switching and high power densities, as confirmed by the including inductive heating and battery charging [1], [2] context, to cite a few. Their conventional control includes frequency and amplitude modulation, typically relying on small signal models, which are dependent on the operating point. Early works focus their attention on unifying the characterization of several topologies using high-order models, which are then analyzed using first-harmonic approaches or linearization [3], [4]. As an alternative, several state plane-based approaches have been proposed, where the input switching is derived from current and voltage measurements in the converter. In state-plane control approaches, the dynamics can be simpler, streamlining the design of controllers, which can show improved regulation performance and a more immediate hardware realization. Some of these approaches drive the resonant converter in a self-oscillating way, without the need of external oscillators. One of the inherent advantages of self-oscillation is that the converter can be operated at the resonant frequency with no compensation for parameters variations in the components of the resonant tank. State-plane trajectories were used in [5] to describe the steady-state operating point with conventional controllers, but the potential of state plane-based switching was only explored in follow up works. A

This work has been partially sponsored by the Spanish Ministry of Science and Innovation under project PID2019-111443RB-I00, by the international exchange program of the University of Trento (Italy), and by ANR via grant HANDY, number ANR-18-CE40-0010. (*Corresponding author: Nicola Zaupa.*)

Nicola Zaupa was with Department of Industrial Engineering, Università di Trento, 38122 Trento, Italy. He is now with CNRS-LAAS, Université Toulouse III, 31400 Toulouse, France. (e-mail: nicola.zaupa@laas.fr).

Luis Martínez-Salamero and Carlos Olalla are with the Departament d'Enginyeria Electrònica, Elèctrica i Automàtica, Escola Tècnica Superior d'Enginyeria, Universitat Rovira i Virgili, 43007 Tarragona, Spain (e-mail: luis.martinez@urv.cat; carlos.olalla@urv.cat).

Luca Zaccarian is with CNRS-LAAS, Université de Toulouse, 31400 Toulouse, France, and also with Department of Industrial Engineering, Università di Trento, 38122 Trento, Italy (e-mail: zaccarian@laas.fr).

trajectory tracking approach is used in [6], where no self-oscillating mechanism is exploited. Self-oscillation is instead adopted in [7], where a state plane-based solution is proposed, based on two controllers: one for the startup and one for the steady-state. The stability of the induced limit cycle with the switching mechanism for the start-up is analyzed in [8] with a Poincaré map. Further developments in that direction include [9]–[11] that analyze series resonant converters with switched affine models, followed by [12]–[14] that demonstrate that state-plane based methods can outperform the dynamics of conventional approaches. Nonetheless, the above state-plane control solutions also have limitations, one of them (resolved here) being the assumption that the resonant tank has a sufficiently high quality factor Q [12], [14].

For providing rigorous guarantees, a full nonlinear dynamics perspective on these ON-OFF type of feedbacks naturally calls for the use of a hybrid dynamical systems formalism: an area where powerful stability analysis tools have been recently developed in [15] with a Lyapunov approach. Several relevant power electronics challenges have been addressed with these tools recently, such as the hybrid control of inverters in [16], [17] and DC-DC converters in [18]–[21]. Nonetheless, these approaches are not applicable to resonant conversion, where the switching frequency does not correspond to a small ripple, but to the main AC component of the power transfer.

In our preliminary conference results [22], we proposed a novel unifying second-order input-dependent (or hybrid) coordinate transformation to analyze the dynamics of second-order parallel and series resonant converters (PRC, SRC). Differently from the phasor circuit-based steady-state analysis leading to the high-order unifying models in [3], [4], our state-plane low-dimensional coordinates allow specifying a state-plane control law based on a reference input corresponding to an angle $\theta \in (0, \pi]$, identifying suitable sectors in this new hybrid coordinate system, independently of the load. It is worth pointing out that thanks to the proposed approach the dynamics are unified, but not in the sense of a unique model that can be particularized for different cases. The proposed change of coordinates describes both converters with the same dynamics equations and without increasing their order. Different from the two-controllers scheme of [7], our self-oscillating solution only requires one controller. Moreover, our self-oscillation mechanism overcomes the stringent bound on the quality factor assumed in [12], [14]: our only mild requirement on the quality factor is that the dynamics of the resonant tank must be underdamped. In [22], we also discussed in depth the PRC configuration, showing a desirable dependence of the output amplitude and frequency on the reference input θ . We also proved rigorously the existence of a unique nontrivial hybrid limit cycle, but only for the

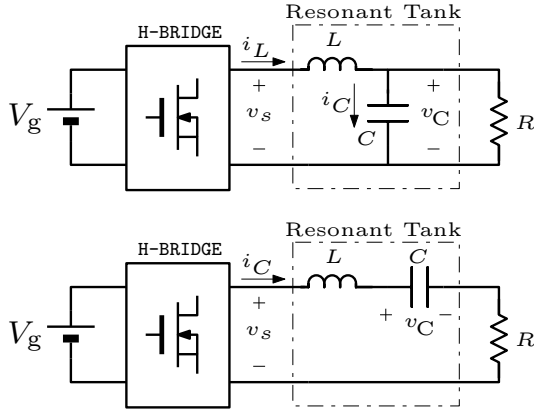


Fig. 1. Circuits associated with the parallel resonant converter (PRC, top) and series resonant converter (SRC, bottom).

specific case $\theta = \frac{\pi}{2}$, leaving the same result for the whole range $\theta \in (0, \pi]$ as a conjecture.

In this work we extend [22] in several important directions: first, we generalize the main theorem of [22] about the existence of the unique limit cycle and our new proof, based on a different Lyapunov argument, applies to any reference $\theta \in (0, \pi]$. Then, while [22] only reported simulation results, we report here on the development of an experimental device implementing our feedback on a SRC architecture. Finally, since only the PRC solution was simulated in [22], we perform SRC simulations here and show desirable matching of the simulation and experimental results.

The paper is structured as follows. The unifying coordinate representation is presented in Section II and the related hybrid system in Section III. Section IV states and proves our main theoretical result and Section V contains the controller implementation. The experimental prototype is described in Section VI with comparative simulations and experiments.

Notation. \mathbb{R} ($\mathbb{R}_{>0}$) [$\mathbb{R}_{\geq 0}$] and \mathbb{Z} ($\mathbb{Z}_{>0}$) [$\mathbb{Z}_{\geq 0}$] are the sets of (positive) [non-negative] real and integer numbers. \mathbb{R}^n denotes the n -dimensional Euclidean space. Given two vectors $u \in \mathbb{R}^n$ and $w \in \mathbb{R}^m$, u^\top denotes the transpose of u , and $(u, w) := [u^\top w^\top]^\top$ denotes their stacking. Given a (continuous, discrete, or hybrid) signal x , \dot{x} denotes its derivative with respect to continuous time t , while x^+ denotes its next value with respect to discrete time j .

II. UNIFYING INPUT-DEPENDENT COORDINATE CHANGES

We address parallel and series resonant converters (PRC and SRC, respectively), whose circuits are shown in Fig. 1, where v_C and i_C denote the voltage and the current in the capacitor. Both configurations exhibit a (parallel or series) resonant tank driven by an H-bridge applying a supply voltage v_s equal to either V_g or $-V_g$ to the left terminal, where V_g is an external DC supply. The H-bridge is modeled here by a binary variable $\sigma \in \{-1, 1\}$ describing the switch position, so that $v_s = V_g$ when $\sigma = 1$ and $v_s = -V_g$ when $\sigma = -1$ (in summary $v_s = \sigma V_g$).

The linear equations governing the current and voltage evolution of v_C and i_C for the parallel configuration at the top of Fig. 1 are the following ones:

$$L \frac{di_L}{dt} = \sigma V_g - v_C, \quad C \frac{dv_C}{dt} = i_L - \frac{v_C}{R}. \quad (1)$$

We emphasize that the last term, $(i_L - \frac{v_C}{R})$, is the current i_C flowing in the capacitor. Similarly, the linear equations governing the series configuration at the bottom of Fig. 1 correspond to:

$$L \frac{di_L}{dt} = \sigma V_g - v_C - Ri_L, \quad C \frac{dv_C}{dt} = i_C. \quad (2)$$

Note that in this case $i_L = i_C$. The novel approach proposed there stems from introducing the next input-dependent quantities for the converters

$$z_1 := \frac{v_C}{V_g} - \sigma, \quad z_2 := \frac{1}{V_g} \sqrt{\frac{L}{C}} i_C, \quad (3)$$

the first one clearly corresponding to a transformed voltage and the second one being a transformed current.

Keeping in mind that any variation of $\sigma \in \{-1, 1\}$ must be instantaneous, so that $\dot{\sigma} = 0$, we may compute the differential equations governing the evolution of variables $z := (z_1, z_2)$ in (3). As shown in [22], the dynamics is the same for the two circuits and corresponds to the following damped oscillator

$$\dot{z}_1 = \omega z_2, \quad \dot{z}_2 = -\omega z_1 - \beta z_2, \quad (4)$$

where $\omega := (\sqrt{LC})^{-1}$ is the natural frequency and $\beta > 0$ is the inverse of the time constant of the exponential decay associated with each one of the linear circuits:

$$\beta_{\text{PRC}} := \frac{1}{RC}, \quad \beta_{\text{SRC}} := \frac{R}{L}. \quad (5)$$

Since the coordinates (z_1, z_2) depend on the input σ , they experience an instantaneous change when σ is toggled. In particular, since σ toggles between -1 and $+1$, namely $\sigma^+ = -\sigma$, then (3) provides, for both circuits:

$$(z_1^+, z_2^+, \sigma^+) = (z_1 + 2\sigma, z_2, -\sigma), \quad (6)$$

where we emphasize that σ represents the switch position before the update and σ^+ represents its position after the update (and similarly for the other variables).

III. HYBRID MODEL AND PROPOSED SWITCHING LAW

Summarizing the previous section we may build a hybrid model of both PRC and SRC, with the notation of [15] where $z = (z_1, z_2) \in \mathbb{R}^2$ is a physical state related to the current and voltage in the circuit, and $\sigma \in \{-1, 1\}$ is a logical state representing the position of the switch:

$$\begin{bmatrix} \dot{z} \\ \dot{\sigma} \end{bmatrix} = f(z, \sigma) := \begin{bmatrix} Az \\ 0 \end{bmatrix} \quad (z, \sigma) \in \mathcal{C}(\theta) \quad (7a)$$

$$\begin{bmatrix} z^+ \\ \sigma^+ \end{bmatrix} = g(z, \sigma) := \begin{bmatrix} z + \begin{bmatrix} 2\sigma \\ 0 \end{bmatrix} \\ -\sigma \end{bmatrix} \quad (z, \sigma) \in \mathcal{D}(\theta), \quad (7b)$$

where $A := \begin{bmatrix} 0 & \omega \\ -\omega & -\beta \end{bmatrix}$, $\omega := (\sqrt{LC})^{-1} > 0$ is the natural frequency of the converter and $\beta > 0$ suitably defined based on

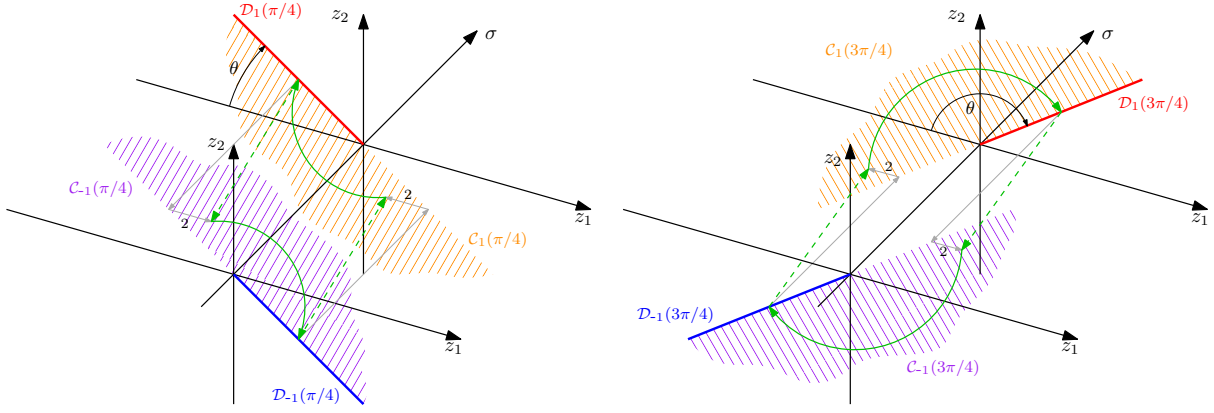


Fig. 2. Two possible solutions of system (7), (8) with $\theta < \frac{\pi}{2}$ (left) and $\theta > \frac{\pi}{2}$ (right).

the PRC or SRC configuration (see (5)) represents the internal dissipation.

The sets \mathcal{C} and \mathcal{D} in (7) are called, respectively, “flow set” and “jump set” and they are suitable subsets of $\mathbb{R}^2 \times \{-1, 1\}$ to be designed in this section. Their intuitive meaning is that whenever the (augmented) state $\xi := (z, \sigma)$ belongs to \mathcal{D} , it is time to change the switch position in the H-bridge driving the converter, whereas as long as $\xi \in \mathcal{C}$, one may let the converter evolve continuously without changing the switch position.

As a consequence, the selection of \mathcal{C} and \mathcal{D} implicitly defines a feedback controller because it characterizes under what conditions the converter input should be toggled (or left unchanged). In this section we design \mathcal{C} and \mathcal{D} as in [22], based on a reference input $\theta \in (0, \pi]$ (called “switching angle” in [22]) capable of inducing different output amplitudes and frequencies in the self-oscillating behavior. We select the jump and flow sets as:

$$\begin{aligned} \mathcal{C}(\theta) &:= \mathcal{C}_1(\theta) \cup \mathcal{C}_{-1}(\theta), \\ \mathcal{D}(\theta) &:= \mathcal{D}_1(\theta) \cup \mathcal{D}_{-1}(\theta). \end{aligned} \quad (8a)$$

where each set \mathcal{C}_1 and \mathcal{C}_{-1} denotes a half plane and \mathcal{D}_1 and \mathcal{D}_{-1} are two half lines delimiting the flow sets, namely for each $q \in \{1, -1\}$,

$$\mathcal{C}_q(\theta) := \{(z, \sigma) : \sigma = q, \sigma(z_1 \sin \theta + z_2 \cos \theta) \leq 0\}, \quad (8b)$$

$$\mathcal{D}_q(\theta) := \{(z, \sigma) : \sigma = q, \sigma z_2 \geq 0, z_1 \sin \theta + z_2 \cos \theta = 0\}. \quad (8c)$$

Two possible closed-loop solutions induced by (8) are illustrated in Fig. 2, where they evolve in the three-dimensional state-space (z_1, z_2, σ) . The left figure represents a scenario with the reference $\theta < \frac{\pi}{2}$ while the right figure corresponds to $\theta > \frac{\pi}{2}$. During flowing (in $\mathcal{C}(\theta)$), the continuous evolution revolves in the clockwise direction. Switching always occurs when the continuous motion hits the tilted solid line, because from that line flowing in $\mathcal{C}(\theta)$ is not possible, unless the state σ is toggled. When a switch occurs, the z_1 voltage is shifted horizontally by two units (see (6)), and the specific choice of $\mathcal{C}(\theta)$ and $\mathcal{D}(\theta)$ ensures that those shifts always map to the interior of $\mathcal{C}(\theta)$, from where flowing should occur. The choice to split \mathcal{D} in two half lines regularizes the domain avoiding Zeno solutions with $\theta = \pi$. The angle θ controls the tilting

of the solid line, namely the subspace where the switch takes place. It is apparent that with small values of θ (left case in Fig. 2) solutions flow only in a small portion of the phase plane while for larger values of θ flowing is allowed in a larger range of phases, up to the limit case $\theta = \pi$, where the solution spans all the possible phases while flowing.

IV. ASYMPTOTICALLY STABLE HYBRID LIMIT CYCLE

A. Main Stability Theorem

According to [23], the notion of periodicity for a hybrid trajectory is reported below. Alternative equivalent definitions are given in [24].

Definition 1 Given an hybrid system $\mathcal{H} = (\mathcal{C}, f, \mathcal{D}, g)$, a nontrivial hybrid periodic trajectory φ is a complete solution (namely, a solution that evolves forever) that is not identically zero and for which there exists a pair $(T, J) \in \mathbb{R}_{\geq 0} \times \mathbb{Z}_{\geq 0}$ satisfying $T + J > 0$, such that $(t, j) \in \text{dom}(\varphi)$ implies $(t + T, j + J) \in \text{dom}(\varphi)$ and, moreover,

$$\varphi(t, j) = \varphi(t + T, j + J) \quad (9)$$

The image of φ is a nontrivial hybrid periodic orbit.

The next assumption on the parameters of (7) is necessary for the existence of a nontrivial hybrid periodic trajectory.

Assumption 1 Parameters ω and β are strictly positive reals. Moreover, the relation $\beta < 2\omega$ is satisfied, namely the resonant tank is underdamped. Equivalently, the roots of $s^2 + \beta s + \omega^2 = 0$ are complex conjugate.

The following theorem, whose proof is reported in Section IV-B, provides a justification for the proposed self-oscillating control law. In our preliminary work [22] we reported its proof only for the case $\theta = \frac{\pi}{2}$. We prove it here for any value of $\theta \in (0, \pi]$.

Theorem 1 Under Assumption 1, for each selection of $\theta \in (0, \pi]$, the closed loop (7), (8) has a unique nontrivial hybrid periodic orbit \mathcal{O}_θ that is stable and almost globally attractive (its basin of attraction includes all points such that $z \neq 0$).

Moreover, the nontrivial hybrid periodic trajectories of (7), (8) are characterized by $J = 2$ and $T(\theta) > 0$, and exhibit periodic jumps interlaced by flowing intervals of length $T(\theta)/2$.

Remark 1 Assumption 1 imposes constraints on the physical components to ensure that a natural oscillatory motion occurs, as certified by Theorem 1. For the two circuit configurations in Fig. 1, the constraint $\beta < 2\omega$ corresponds to:

$$\text{PRC} : 2R > \sqrt{\frac{L}{C}} \quad \text{SRC} : \frac{R}{2} < \sqrt{\frac{L}{C}}. \quad (10)$$

Requirements (10) are reasonable since the effect of the load R must be sufficiently small to not destroy the natural oscillatory behavior of the LC resonant network. Ideally one would want, $R \rightarrow \infty$ (open circuit) for the PRC and $R \rightarrow 0$ (short circuit) for the SRC. Both conditions in (10) can be stated in terms of quality factor Q . Considering that $Q_{\text{PRC}} = R\sqrt{\frac{C}{L}}$ and $Q_{\text{SRC}} = \frac{1}{R}\sqrt{\frac{L}{C}}$ we have that:

$$Q = \frac{\omega}{\beta} > 0.5, \quad (11)$$

which interestingly corresponds to the same requirement for both architectures. Constraint (11) immediately shows the advantage of our novel switching law, as compared to the alternative solutions of [12], [13]. Indeed, a nontrivial discussion is present in [12] showing for the PRC case that with $Q < 3.15$ there is no guarantee of a self-oscillating behavior (the controller in [12] may reach an equilibrium). The result of Theorem 1, only requiring the mild assumption (11) provides an important improvement. \circ

Remark 2 The flow and jump sets of hybrid dynamics (7), (8) are closed, and the flow and jump maps are continuous functions, therefore (7), (8) enjoys the so-called hybrid basic conditions of [15, As. 6.5]. This, among other things, implies robustness of asymptotic stability of compact attractors, as characterized in [15, Ch. 7]. A consequence of robustness is that one expects a graceful degradation of the closed-loop stability properties (the so-called semiglobal practical robustness): an important feature for the experimental results discussed in Sections V and VI. \circ

B. Hybrid Lyapunov function and proof of Theorem 1

In this section we prove Theorem 1, based on hybrid Lyapunov theory [15]. Our proof shares interesting similarities with the approach reported in [25] (see also [23]), which address relay-based control of mechanical systems. In particular for the case $\theta = \frac{\pi}{2}$ it is shown in [22] that Theorem 1 immediately follows from [25]. Here we provide nontrivial derivations to allow extending the result to any $\theta \in (0, \pi]$.

Before proving Theorem 1, let us recall from [26, Def. 5.1] that a function $\psi : \mathbb{R} \rightarrow \mathbb{R}$ is α -strongly convex if and only if there exists $\alpha > 0$ such that for each $a, b \in \mathbb{R}$ it holds that

$$\psi(a) - \psi(b) \geq \sigma(a - b) + \frac{\alpha}{2}|a - b|^2, \quad \forall \sigma \in \partial\psi(b), \quad (12)$$

where $\partial\psi(b) \subset \mathbb{R}$ is the subdifferential of ψ at b .

Based on (12) we can prove the following lemma, which is instrumental for the proof of Theorem 1.

Lemma 1 Consider two continuous functions of the scalar variable $\xi \in \mathbb{R}_{\geq 0}$. A linear function $\xi \mapsto \psi_1(\xi) = \psi_0 + \gamma\xi$, with $\psi_0, \gamma \in \mathbb{R}$, and a strongly convex function ψ_2 with $\psi_2(0) < \psi_0$. Function $\xi \mapsto \psi_1(\xi) - \psi_2(\xi)$ grows unbounded as $\xi \rightarrow +\infty$ and has exactly one zero for $\xi \geq 0$.

Proof. Denote $\tilde{\psi}(\xi) := \psi_2(\xi) - \psi_1(\xi)$ and note that it is strongly convex because, for each $a, b \in \mathbb{R}$ and each $\sigma \in \partial\psi_2(b)$, it satisfies, from (12) applied with $\psi = \psi_2$,

$$\begin{aligned} \tilde{\psi}(a) - \tilde{\psi}(b) &= \psi_2(a) - \psi_2(b) - \gamma(a - b) \\ &\geq \tilde{\sigma}(a - b) + \frac{\alpha}{2}|a - b|^2, \end{aligned} \quad (13)$$

where $\tilde{\sigma} = \sigma - \gamma$ characterizes any vector in the subdifferential of $\tilde{\psi}$ at b .

Let us first prove that function $\tilde{\psi}$ has at least one zero for $\xi \in [0, +\infty)$. From $\psi_1(0) = \psi_0 > \psi_2(0)$, we have $\tilde{\psi}(0) < 0$. Applying (13) at the unique global minimum ξ^* (wherein $\tilde{\sigma} = 0$ belongs to $\partial\tilde{\psi}(\xi^*)$), we have $\tilde{\psi}(\xi) \geq \tilde{\psi}(\xi^*) + \frac{\alpha}{2}|\xi - \xi^*|^2$, which proves that $\lim_{\xi \rightarrow +\infty} \tilde{\psi}(\xi) = +\infty$, showing unbounded-

ness of $\psi(\xi)$ as $\xi \rightarrow +\infty$. Moreover, with $\tilde{\psi}(0) < 0$ and continuity, there exists at least one ξ_0 where $\tilde{\psi}(\xi_0) = 0$.

Let us now prove that ξ_0 is unique. Assume that there are two points $0 < \xi_0 < \xi_1$ where $\tilde{\psi}$ is zero and fix $a = \xi_1, b = \xi_0$. Then from (13) with these selections, we get:

$$0 > \tilde{\sigma}(\xi_1 - \xi_0) + \frac{\alpha}{2}|\xi_1 - \xi_0|^2, \quad (14)$$

which clearly implies $\tilde{\sigma} < 0$. Since $\tilde{\sigma} \in \partial\tilde{\psi}(\xi_0)$ and $\tilde{\psi}(\xi_0) = 0$, by definition of subdifferential, using $0 < \xi_0$, we have $\tilde{\psi}(0) \geq \tilde{\psi}(\xi_0) - \tilde{\sigma}\xi_0 = -\tilde{\sigma}\xi_0 > 0$, which is a contradiction, because we proved above that $\tilde{\psi}(0) < 0$. \blacksquare

For proving Theorem 1, we formulate the following corollary of [25, Lemma 1], relating the dissipated energy along a flowing solution of (7), (8) to the hatched area in Fig. 3 (right).

Lemma 2 Consider any solution z to (7), (8) flowing from \mathcal{G}_1 at ordinary time t_1 to \mathcal{D}_1 at ordinary time $t_2 > t_1$ and define energy-like function $E(z) = \frac{1}{2}z_1^2 + \frac{1}{2}z_2^2 = \frac{1}{2}|z|^2$. The dissipated energy $E(z(t_2)) - E(z(t_1))$ is equal to $\frac{\beta}{\omega}\Pi$, where Π is the (unsigned) area hatched between the graph of the trajectory $z(t)$, $t \in [t_1, t_2]$ and the coordinate axis $z_2 = 0$.

Proof. Consider the following selection of the parameters and states in [25]

$$x_1 = z_1, \quad x_2 = \omega z_2, \quad m = 1, \quad c = \beta, \quad k = \omega^2. \quad (15)$$

From [25, Lemma 1] the function $E_{[21]}(x) = \frac{1}{2}\omega^2 x_1^2 + \frac{1}{2}x_2^2 = \omega^2 E(z)$ dissipates $\Delta E_{[21]} = \beta\Pi_{[21]}$ between t_1 and t_2 . From (15), in the z coordinates we have $\Pi_{[21]} = \omega\Pi$ and since $\Delta E_{[21]} = \omega^2\Delta E$, we have $\Delta E = \frac{1}{\omega^2}\Delta E_{[21]} = \frac{\beta}{\omega^2}\Pi_{[21]} = \frac{\beta}{\omega}\Pi$ as to be proven. \blacksquare

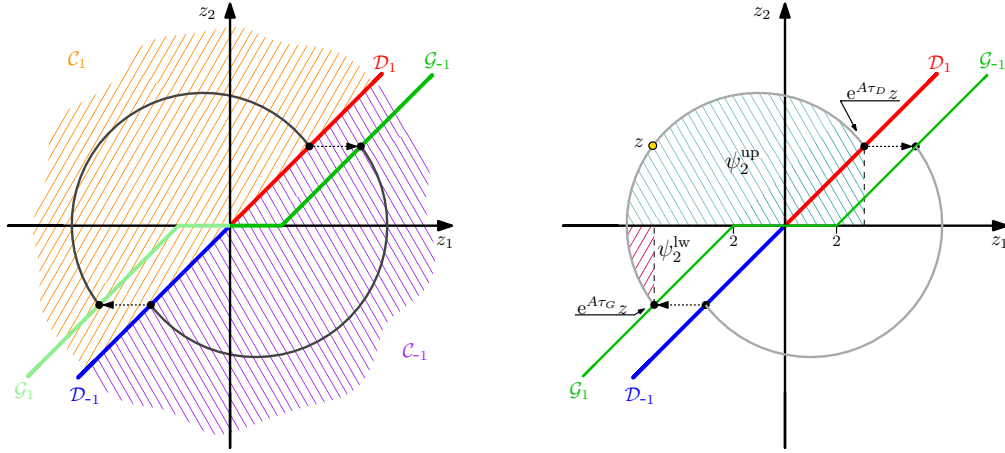


Fig. 3. Evolution of solutions and sets \mathcal{G}_1 (in green) and \mathcal{D}_1 (in red) discussed in the proof of Theorem 1.

To construct a Lyapunov function proving Theorem 1, let us only consider the half-space \mathcal{C}_1 , which also contains \mathcal{D}_1 (parallel definitions apply to \mathcal{C}_{-1}) and introduce the set

$$\begin{aligned} \mathcal{G}_1 := & \{z \in \mathcal{C}_1 : z_2 \leq 0, (z_1 + 2) \sin \theta + z_2 \cos \theta = 0\} \cup \\ & \{z \in \mathcal{C}_1 : z_1 \in [-2, 0], z_2 = 0\}, \end{aligned} \quad (16)$$

which corresponds to the green-colored half line parallel to \mathcal{D}_{-1} in Fig. 3. Then, for each point $z \in \mathcal{C}_1 \setminus \{0\}$, denote the compact time interval associated with the unique backward and forward flowing solutions of (7), flowing in \mathcal{C}_1 , as

$$\mathcal{T}_1(z) := \{\tau \in \mathbb{R} : e^{A\tau} z \in \mathcal{C}_1, \forall s \in [\tau, 0] \cup [0, \tau]\}, \quad (17)$$

where $[t_2, t_1]$ should be understood as the empty set when $t_2 > t_1$, so that $[\tau, 0] \cup [0, \tau]$ always describes an interval containing zero, whether τ is positive or negative. Clearly, $0 \in \mathcal{T}_1(z)$ for all $z \in \mathcal{C}_1 \setminus \{0\}$. Based on $\mathcal{T}_1(z)$, define the following two times, which exist and are unique for each $z \in \mathcal{C}_1 \setminus \{0\}$ due to the revolving nature of solutions, as per Assumption 1:

$$\tau_G(z) := \{\tau \in \mathcal{T}_1(z) : e^{A\tau} z \in \mathcal{G}_1\}, \quad (18)$$

$$\tau_D(z) := \{\tau \in \mathcal{T}_1(z) : e^{A\tau} z \in \mathcal{D}_1\}. \quad (19)$$

The Lyapunov function proposed in this proof, which is represented in Fig. 4 for the special case $\theta = 3\pi/4$, is based on (18), (19) and corresponds to

$$V(z) := \max\{\tau_G(z), 0\} + \frac{(\delta_V(z) - \frac{\beta}{\omega} \Pi(z))^2}{([1 \ 0] e^{A\tau_G(z)} z)^2}, \quad (20)$$

$$\delta_V(z) := 2 \left(1 + \sigma [1 \ 0] e^{A\tau_D(z)} z\right), \quad (21)$$

where $\Pi(z)$ has been defined in Lemma 2.

The first term of $V(z)$ in (20) is positive when z lies in the stripe between the set \mathcal{D}_{-1} and \mathcal{G}_1 of Fig. 3, wherein $\tau_G(z) > 0$, but it is zero in the remaining points of \mathcal{C}_1 , wherein $\tau_G(z) \leq 0$. The second term of $V(z)$ is inspired by [25]. Referring to the energy E defined in Lemma 2, its numerator corresponds to the difference between the dissipated energy $\frac{\beta}{\omega} \Pi(z)$ (sampled in a Poincaré fashion) along the flow from \mathcal{G}_1 to \mathcal{D}_1 with the increase of energy across the jump from $z_{1,D} = [1 \ 0] e^{A\tau_D(z)} z$, which belongs to \mathcal{D}_1 , namely

$$\delta_V(z) = \frac{1}{2}((z_{1,D}^+)^2 - z_{1,D}^2) = 2(1 + \sigma z_{1,D}), \quad (22)$$

as defined in (21). Note that by construction Π and δ_V are constant along flowing solutions, therefore, whenever $\tau_G(z) \leq 0$, V remains constant along flowing solutions. Comparing $\delta_V(z)$ with $\frac{\beta}{\omega} \Pi(z)$, an energy balance between flows and jumps emerges when $\delta_V(z) - \frac{\beta}{\omega} \Pi(z) = 0$, that is when $V(z) = 0$. The denominator of the right term in (20) simply ensures that, close to the origin, V blows up to infinity, as it should because the origin is a weak equilibrium (it admits a constant flowing solution not converging to the hybrid periodic orbit) and cannot belong to the basin of attraction.

Defining $V(z)$ in a parallel way for $z \in \mathcal{C}_{-1}$, we prove below that the following set, the zero level set of V , corresponds to the set \mathcal{O}_θ characterized in Theorem 1:

$$\mathcal{A} := \{(z, \sigma) : \delta_V(z) = \frac{\beta}{\omega} \Pi(z), \text{ and } \tau_G(z) \leq 0\}, \quad (23)$$

with δ_V defined in (21). We are now ready to prove Theorem 1.

Proof of Theorem 1 Let us first characterize function Π , which is constant by construction along flowing solutions. Due to this fact we can parametrize all values of $\Pi(z)$, $z \in \mathcal{C} \cup \mathcal{D}$, following a Poincaré approach for each $z \in$

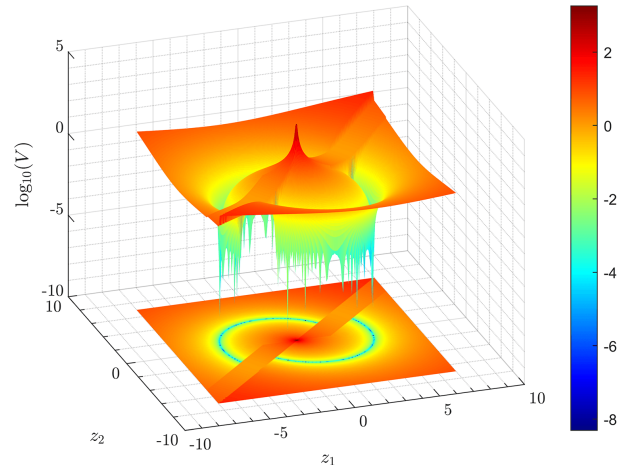


Fig. 4. Logarithmic representation of the Lyapunov function V in (20), for the value $\theta = 3\pi/4$.

\mathcal{D}_1 , via $\Pi(z) = \psi_2(|z|)$, where $\psi_2(|z|)$ is the sum of the upper area $\psi_2^{\text{up}}(|z|) = \alpha^{\text{up}}|z|^2$, which is homogeneous of degree two by construction, and the lower area $\psi_2^{\text{lw}}(|z|) = \alpha^{\text{lw}} \max\{|z| - |z_0|, 0\}^2$, with $z_0 \in \mathcal{D}$ being the unique point such that $e^{A\tau_G(z_0)}z_0 = \begin{bmatrix} -2 \\ 0 \end{bmatrix}$, namely the point where \mathcal{G}_1 has a kink, in Fig. 3. Due to homogeneity of the linear solutions (larger solutions are scaled versions of the smallest ones), it is immediate to see that $\psi_2^{\text{lw}}(|z|)$ is (non-strictly) convex and $\psi_2^{\text{up}}(|z|)$ is strongly convex. Therefore their sum is strongly convex. Let us continue by observing that for each $z \in \mathcal{D}_1$, we can express the injected energy as

$$\psi_1(|z|) := |z^+|^2 - |z|^2 = 2(1 - |z| \cos \theta) = \delta_V(z). \quad (24)$$

Then, from Lemma 1, there exists only one positive value $\xi^* = |z^*|$ of $|z|$ leading to the energy balance $\psi_2(|z^*|) = \psi_1(|z^*|)$. In particular, the hybrid periodic orbit \mathcal{O}_θ corresponds to the image of the hybrid periodic trajectory starting at the unique point $z^* \in \mathcal{D}_1$.

By uniqueness of z^* , the nontrivial hybrid periodic orbit \mathcal{O}_θ is unique and coincides with set \mathcal{A} in (23).

Let us now prove the asymptotic stability of \mathcal{A} with basin of attraction $\mathcal{B}_\mathcal{A} = (\mathbb{R}^2 \setminus \{0\}) \times \{-1, 1\}$. To this end, let us first note that V is zero in \mathcal{A} , positive in $\mathcal{B}_\mathcal{A}$ and, from Lemma 1, radially unbounded, relative to the open set $\mathcal{B}_\mathcal{A}$, with respect to \mathcal{A} . Moreover, since the points $e^{A\tau_D(z)}z$ and $e^{A\tau_G(z)}z$ remain constant along flowing solutions and $\tau_G(z)$ is a decreasing function of time (due to the revolving nature of the solutions stemming from Assumption 1), then V in (20) is nonincreasing when flowing in \mathcal{C} . Finally, from Lemma 1, and using similar arguments to those of [25, Lemma 2], the Lyapunov function decreases across jumps. More specifically, the following weak Lyapunov properties hold

$$\begin{aligned} \dot{V} &:= \langle \nabla V(z), f(z, \sigma) \rangle \leq 0, \quad \forall (z, \sigma) \in \mathcal{C} \setminus (\{0\} \times \{-1, 1\}), \\ \Delta V &:= V(g(z, \sigma)) - V(z) < 0, \quad \forall (z, \sigma) \in \mathcal{D} \setminus \mathcal{A}. \end{aligned}$$

As in [25], the asymptotic stability of \mathcal{A} with basin of attraction $\mathcal{B}_\mathcal{A}$ then follows from the nonsmooth hybrid invariance principle of [27, Thm 1].

The proof is completed by noting that, except for the trivial flowing solution at zero, the hybrid limit cycle whose orbit is \mathcal{A} , is globally attractive and therefore it is the only possible one. Moreover, due to the symmetry of the flow/jump sets and maps, this cycle is associated with periodic jumps, where the period $T(\theta)$ of the jumps is given by the time it takes for a solution to reach \mathcal{D}_1 from \mathcal{G}_1 , along the periodic orbit. The period of the limit cycle is $(2T(\theta), 2)$ because, by construction, it takes two half revolutions for the periodic trajectory starting in from \mathcal{G}_1 to revisit the same point in \mathcal{G}_1 . ■

V. CONTROLLER IMPLEMENTATION

This section discusses the practical implementation of the hybrid switching law, which has been verified with high fidelity simulations in PSIM software.

Implementing the hybrid feedback requires making a decision about whether a switch should be performed or not, based on the jump/flow sets. An analog-based solution could check the flow/jump conditions in the continuous time domain, as

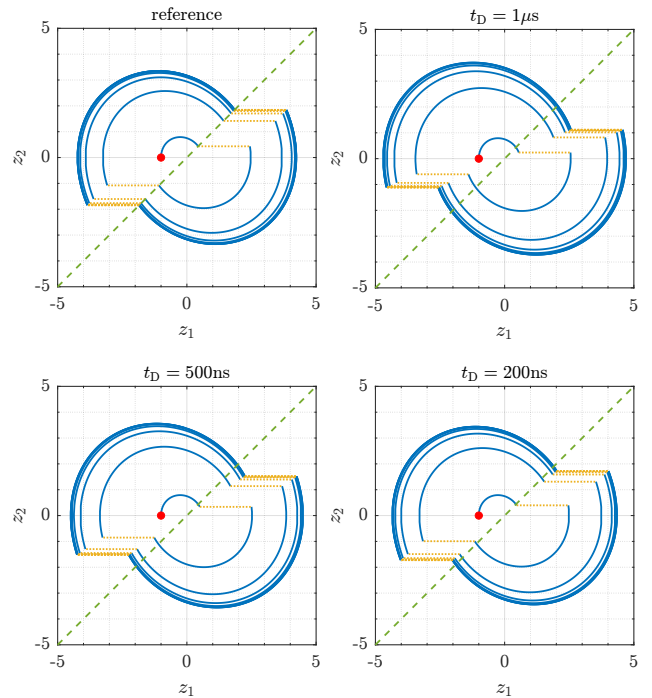


Fig. 5. Comparison between the simulated response with an analog implementation (top-left) with the sampled-data implementation, with different delays t_D and using a constant switching angle $\theta = 3\pi/4$.

in [20], such that there is no information loss, at the expense of a relatively complex tuning and a rigid design reuse. On the other hand, a digital alternative would facilitate complex calculations and reprogramming capability, at the expense of some information loss due to the analog-to digital converters (ADCs) and the presence of a time-delay in the control loop. Information loss in digitally controlled power converters is caused by the digital pulse width modulator (PWM) and the quantization error of the analog to digital converter (ADC), which may generate undesired oscillations [28]. In turn, time-delay negative effects can be mitigated by performing the sampling/conversion process at a fast sampling rate, up to more than 30 times the switching frequency [29]. In this work, the hybrid control is digitally implemented because the two above mentioned drawbacks are minimized. Namely, no numerically-induced oscillations emerge because the control strategy does not require a PWM element, and no undesirable delay effects emerge because of the low latency of the FPGA and the high sampling frequency of the ADCs.

This last statement is confirmed by the simulation results reported in Fig. 5, where a delay in the order of 2% (200 ns) of the half period (10 μ s) is acceptable and does not affect significantly the closed-loop response. Fig. 5 reports simulation results for trajectories in the phase-plane (z_1, z_2) when a delay is introduced in the acquisition chain, namely this delay can account for: acquisition time, latency, internal ADC timing. Our discussed theoretical framework actually justifies these robustness features in a rigorous way, thanks to the properties discussed in Remark 2. The results of Fig. 5 confirm that the asymptotic stability is preserved despite the introduction of these perturbations in the feedback loop.

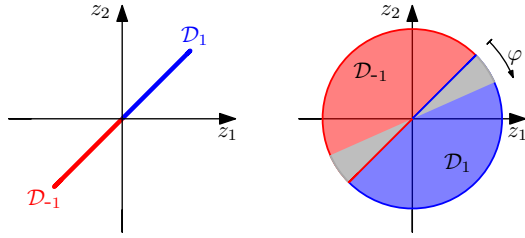


Fig. 6. Representation of the jump sets. The theoretical formulation (left) and the experimental one (right) corresponding to half-plane with time regularization. The shaded areas show the effects of time regularization.

For the measurements of the state $z = (z_1, z_2)$, needed by the feedback controller, it is enough to measure a scaled version of the current and the voltage on the capacitor, as discussed in [22].

The core task of the controller is evaluating the jump condition, to decide whether to switch or not. The introduced jump set formulation (8c) requires checking a zero crossing conditions that can be conveniently extended to a half plane. Moreover, in order to cope with the disturbances arising at the switching instant (which could generate multiple consecutive jumps), time regularization is introduced, which inhibits jumps for t_R seconds, so that the trajectory moves away from the jump set border. We can model this behavior by introducing a timer variable $\lambda > 0$ that is reset to 0 at every jump and linearly increases during flow. Then a jump is allowed only if $\lambda \geq t_R$. The dynamics for λ , which can be added to (7), is

$$\dot{\lambda} = 1 \quad (z, \sigma, \lambda) \in \mathcal{C}_R(\theta), \quad (25a)$$

$$\lambda^+ = 0 \quad (z, \sigma, \lambda) \in \mathcal{D}_R(\theta), \quad (25b)$$

where the time-regularized flow/jump sets are $\mathcal{C}_R(\theta) = \mathcal{C}(\theta) \cup \mathbb{R}_{\geq 0}$ and $\mathcal{D}_R(\theta) = \mathcal{D}(\theta) \cup [t_R, +\infty)$.

A graphical representation of the time-regularized sets is reported in Fig. 6, where the gray area represents the area spanned by the solution while jumps are inhibited. The angular aperture can be approximated with $\varphi = \omega t_R$. As long as t_R is sufficiently small, the results of Theorem 1 also apply with the regularized sets.

VI. EXPERIMENTAL VALIDATION

A. Prototype design

An experimental prototype of an SRC has been developed with target parameters: $f_0 = \frac{\omega}{2\pi} = 50$ kHz, $V_g = 24$ V, and operating power of 100 W. The prototype can be seen in Fig. 7, its schematic is shown in Fig. 8 and the list of components is given in Table I. Frequency is limited to reduce the effect of the sampling-induced delay, even though also industrial prototypes work in this range up to a few hundreds of kHz.

The power stage consists of an H-bridge and a resonant tank. The H-bridge comprises two MOSFET power modules (APTC60AM242G) driven by the IC IR2110. The resonant tank employs a multi-layer ceramic (X7R) 100 nF capacitor and a 94.3 μ H inductor. The sensing is performed with a Hall-effect sensor (CQ-3200) for the current measurements and a differential operational amplifier (NCS2007) for the voltage measurements. Both sensing stages have a low-pass filter to

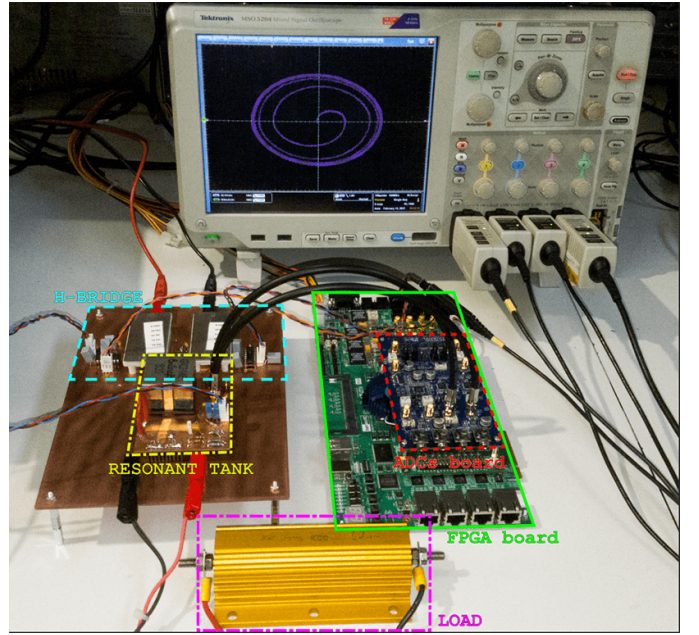


Fig. 7. Picture of the experimental prototype.

TABLE I
SRC PROTOTYPE PARAMETERS.

Parameter	Component	Value
V_g	—	24 V
C_{in}	X7R	1 μ F
M_{1-2}	APTC60AM242G	—
L	AGP4233	100 μ H
C	X7R	100 nF
$C_{L_{PF}}$	poly	10 nF
$C_{H_{PF}}$	poly	100 nF
$R_{L_{PF}}$	trough-hole resistor	50 Ω
$R_{H_{PF}}$	trough-hole resistor	1 k Ω
R_1	trough-hole resistor	270 k Ω
R_2	trough-hole resistor	1.2 k Ω
Driver	IR2110	—
OPAMP	NCS2007	—
Current Sensor	CQ-3200	—
ADC	AD9254	—
FPGA	EP4SGX230KF40C2	—

reduce the noise, additionally the current sensing has a high-pass filter to remove the DC component introduced by the current sensor, which would hinder the operation of the ADC stage.

The controller is implemented in a Stratix IV GX (EP4SGX230KF40C2) FPGA in the DE4 board from Terasic, and its daughter board (AD/DA Data Conversion Card) equipped with AD9254 ADCs operating at 100 MSPS. The high sampling frequency reduces the delay to a negligible value estimated in 200 ns, which is in accordance with the simulation results of Fig. 5.

The converter has been tested with two different loads of 10.1 Ω and 22 Ω , i.e., for quality factors of $Q = 3$ and $Q = 1.4$ respectively. Note that, according to Remark 1, both these situations cannot be addressed with the approach in [12].

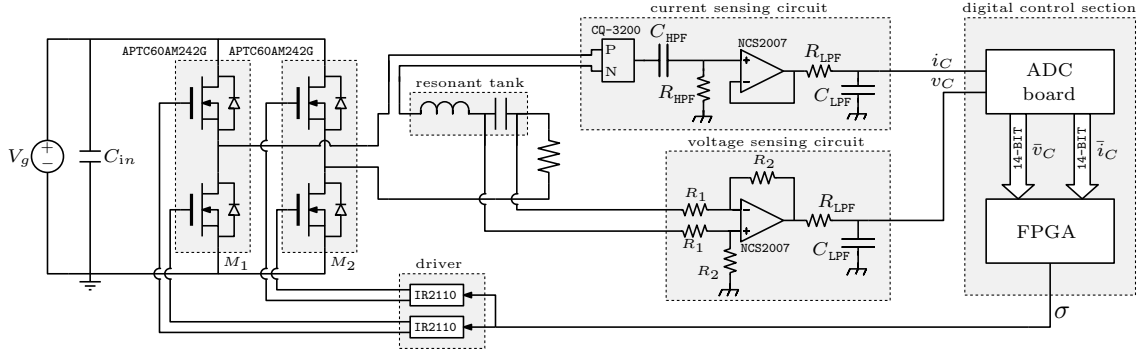


Fig. 8. Schematic of the electronics involved in the prototype including: H-bridge, resonant tank, sensing, controller and drivers.

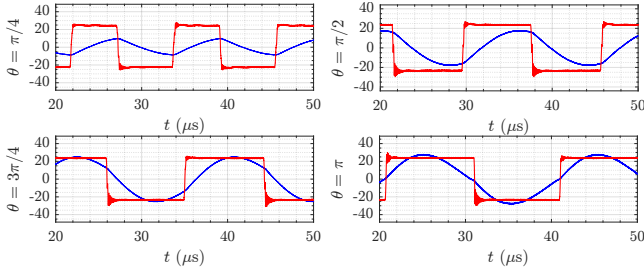


Fig. 9. Inductor current ($\times 10$ A) (blue line) and input voltage v_s (V) (red line) from the prototype for the values of θ shown in Fig. 10.

B. Experimental results

The steady-state input-output waveforms are reported in Fig. 9, showing a desirable output oscillation for various values of θ , thus confirming the result of Theorem 1. Fig. 10 illustrates several simulation (top row) and experimental (bottom row) responses, represented in the (z_1, z_2) phase-plane. In the phase-plane representations, the dotted horizontal segments (yellow and purple) represent the jumps in the trajectories.

Additionally, the converter behavior has been experimentally characterized with respect to the input signal θ . Fig. 11 and Fig. 12 report experimental results compared with the simulation for the two loads. The results show a good match for large values of θ , near the resonance. This is expected because this type of converter typically operates around that region. Fig. 11 and Fig. 12 report the peak of the normalized voltage and the current measured on the capacitor, which have a more meaningful physical interpretation. Indeed, z_2 corresponds to the normalized current $((z_2)_{\text{peak}})$ while z_1 , without the offset introduced by σ , corresponds to the normalized voltage $((z_1)_{\text{peak}} - 1)$. The reported resonant frequencies (dotted black line) are evaluated based on a characterization of the inductance value of the prototype's resonant tank for the two different load conditions. The different values are due to the nonlinear effects of frequency, current and circuit layout on the value of the inductance.

The experiments show good matching with the simulation results for large values of θ , while the discrepancy increases as θ decreases. Experiments with small θ have not been performed due to the high frequency shown by the converter, which makes the self-oscillation harder to sustain with this

controller. Moreover, for small values of θ , the acquired amplitudes were too low with respect to the ADCs input range. These issues reduced the set of angles tested in the prototype, but practically this is not problematic since the converter is supposed to work not far from the resonant frequency. If a larger amplitude variation is needed, other types of controllers should be used, possibly including also operating with zero voltage input ($v_s = 0$).

VII. CONCLUSIONS AND FUTURE DIRECTIONS

We have proposed a unifying coordinate representation for PRC and SRC resonant converters, which leads to a natural feedback control law inducing a unique nontrivial hybrid periodic orbit in a self-oscillating resonant behavior. This resulting hybrid limit cycle has been proved to be almost globally asymptotically stable via a hybrid dynamical systems representation. With the proposed controller, the generation of the limit cycle is ensured in underdamped conditions for any reference input $\theta \in (0, \pi]$, providing a large range of output amplitudes and frequencies, whose trends, as a function of θ , have been characterized. Unlike the self-oscillating mechanism proposed in [12] no high values of Q are required, apart from the underdamped nature of the flow dynamics. Indeed, while in [12] a minimum value of Q was needed to ensure trajectory switching between two equilibrium points, our hybrid switching law only requires complex conjugate poles in the characteristic equation of the linear continuous dynamics. Moreover, the reference input θ is bounded, while in [13] the reference input k goes to infinity for amplitudes near zero. These properties have been experimentally validated on a SRC prototype with a digital implementation of the controller in an FPGA.

Although a feedback loop has been closed to ensure self-oscillation, no regulation of the output current or voltage has been considered. This could be a future direction to investigate, that would require also a dynamic characterization of the hybrid relation between θ and the output amplitudes, in addition to the static characterization done here. Additional future work includes industrial applications such as, for example, battery charging or induction heating. Finally, the hybrid formulation could be extended to higher order resonant converters following similar formulations to those in [12].

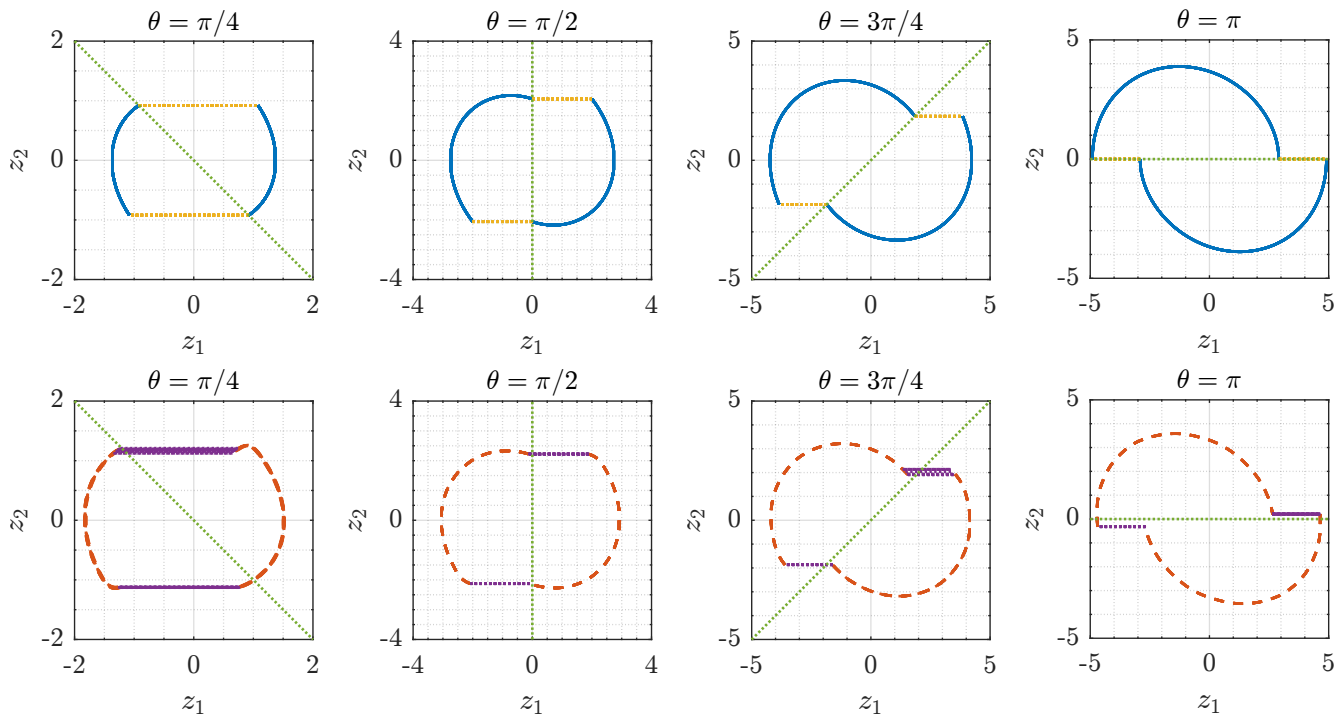


Fig. 10. Phase portraits in the (z_1, z_2) coordinates with different values of θ . Simulation results (top row) and experimental results (bottom row). The θ -tilted dotted green line represents the jumpy set. The load used is $R = 10.1 \Omega$.

REFERENCES

[1] O. Lucía, J. M. Burdío, I. Millán, J. Acero, and L. A. Barragán, “Efficiency-oriented design of ZVS half-bridge series resonant inverter with variable frequency duty cycle control,” *IEEE Transactions on Power Electronics*, vol. 25, no. 7, 2010.

[2] J. Park and S. Choi, “Design and control of a bidirectional resonant DC-DC converter for automotive engine/battery hybrid power generators,” *IEEE Transactions on Power Electronics*, vol. 29, no. 7, 2014.

[3] A. Bhat, “A unified approach for the steady-state analysis of resonant converters,” *IEEE Transactions on industrial electronics*, 1991.

[4] C. Cutrona and C. Di Miceli, “A unified approach to series, parallel and series-parallel resonant converters,” *In Proceedings of 14th International Telecommunications Energy Conference (pp. 139-146)*, 1992.

[5] S. Sooksatra, “A unified approach to the classification and analyses of resonant converters,” *Doctoral dissertation, University of Illinois at Chicago*, 1991.

[6] R. Silva-Ortigoza and H. Sira-Ramírez, “Control of a parallel resonant inverter,” *In 43rd IEEE Conference on Decision and Control*, 2004.

[7] H. Sira-Ramírez and R. Silva-Ortigoza, “On the control of the resonant converter: a hybrid-flatness approach,” *In Proceedings of 15th International Symposium on Mathematical Theory of Networks and Systems*, 2002.

[8] V. Hernández, R. Silva, and H. Sira-Ramírez, “On the stability of limit cycles in resonant dc-to-dc power converters,” *In 42nd IEEE Conference on Decision and Control (pp. 1141-1146)*, 2003.

[9] H. Molla-Ahmadian, A. Karimpour, N. Pariz, and F. Tahami, “Hybrid modeling of a DC-DC series resonant converter: Direct piecewise affine approach,” *IEEE Transactions on Circuits and Systems I: Regular Papers*, vol. 59, no. 12, 2012.

[10] H. Molla-Ahmadian, F. Tahami, A. Karimpour, and N. Pariz, “Hybrid control of DC-DC series resonant converters: The direct piecewise affine approach,” *IEEE Transactions on Power Electronics*, vol. 30, no. 3, 2015.

[11] H. Afshang, F. Tahami, and H. Mollaahmadian, “Hybrid control of the DC-DC series resonant converter operating below resonance,” *IET Power Electronics*, vol. 10, 10 2016.

[12] R. Bonache-Samaniego, C. Olalla, L. Martínez-Salamero, and H. Valderrama-Blavi, “Design of self-oscillating resonant converters based on a variable structure systems approach,” *IET Power Electronics*, vol. 9, no. 1, pp. 111–119, 2016.

[13] R. Bonache-Samaniego, C. Olalla, and L. Martínez-Salamero, “Dynamic modeling and control of self-oscillating parallel resonant converters based on a variable structure systems approach,” *IEEE Transactions on Power Electronics*, vol. 32, no. 2, pp. 1469–1480, 2017.

[14] A. El Aroudi, L. Benadero, E. Ponce, C. Olalla, F. Torres, and L. Martínez-Salamero, “Suppression of undesired attractors in a self-oscillating H-Bridge parallel resonant converters under zero current switching control,” *IEEE Transactions on Circuits and Systems II: Express Briefs*, vol. 66, no. 4, 2019.

[15] R. Goebel, R. Sanfelice, and A. Teel, *Hybrid Dynamical Systems: modeling, stability, and robustness*. Princeton University Press, 2012.

[16] J. Chai and R. Sanfelice, “A robust hybrid control algorithm for a single-phase DC/AC inverter with variable input voltage,” in *Proc. of the 2014 American Control Conference*, 2014, pp. 1420–1425.

[17] L. Torquati, R. Sanfelice, and L. Zaccarian, “A hybrid predictive control algorithm for tracking in a single-phase DC/AC inverter,” in *IEEE Conference on Control Technology and Applications*, Kohala Coast (HI), USA, Aug. 2017, pp. 904–909.

[18] T. A. Theunisse, J. Chai, R. Sanfelice, and W. Heemels, “Robust global stabilization of the DC-DC boost converter via hybrid control,” *IEEE Trans. on Circuits and Systems I: Regular Papers*, vol. 62, no. 4, pp. 1052–1061, 2015.

[19] C. Albea-Sanchez, G. Garcia, S. Hadjeras, W. Heemels, and L. Zaccarian, “Practical stabilisation of switched affine systems with dwell-time guarantees,” *IEEE Transactions on Automatic Control*, vol. 64, no. 11, pp. 4811–4817, 2019.

[20] A. Sferlazza, C. Albea-Sanchez, L. Martínez-Salamero, G. Garcia, and C. Alonso, “Min-type control strategy of a DC-DC synchronous boost converter,” *IEEE Transactions on Industrial Electronics*, 2019.

[21] A. Sferlazza, C. Albea-Sanchez, and G. Garcia, “A hybrid control strategy for quadratic boost converters with inductor currents estimation,” *Control Engineering Practice*, 2020.

[22] N. Zaupa, L. Martínez-Salamero, C. Olalla, and L. Zaccarian, “Results on hybrid control of self-oscillating resonant converters,” in *IFAC Conference on Analysis and Design of Hybrid Systems*, Jul. 2021.

[23] A. Bisoffi, F. Forni, M. Da Lio, and L. Zaccarian, “Relay-based hybrid control of minimal-order mechanical systems with applications,” *Automatica*, vol. 97, pp. 104–114, 2018.

[24] X. Lou, Y. Li, and R. G. Sanfelice, “Robust stability of hybrid limit cycles with multiple jumps in hybrid dynamical systems,” *IEEE Transactions on Automatic Control*, vol. 63, no. 4, pp. 1220–1226, 2018.

[25] A. Bisoffi, F. Forni, M. Da Lio, and L. Zaccarian, “Global results

on reset-induced periodic trajectories of planar systems,” in *European Control Conference*, Jun. 2016, pp. 2644–2649.

- [26] A. Y. Aravkin, J. V. Burke, and D. Drusvyatskiy, “Convex analysis and nonsmooth optimization,” 2017. [Online]. Available: <https://sites.math.washington.edu/~burke/crs/516/notes/graduate-nco.pdf>
- [27] A. Seuret, C. Prieur, S. Tarbouriech, A. Teel, and L. Zaccarian, “A nonsmooth hybrid invariance principle applied to robust event-triggered design,” *IEEE TAC*, vol. 64, no. 5, pp. 2061–2068, 2019.
- [28] A. Peterchev and S. Sanders, “Quantization resolution and limit cycling in digitally controlled pwm converters,” *IEEE Transactions on Power Electronics*, vol. 18, no. 1, pp. 301–308, 2003.
- [29] A. Costabeber, L. Corradini, P. Mattavelli, and S. Saggini, “Time optimal, parameters-insensitive digital controller for DC-DC buck converters,” in *2008 IEEE Power Electronics Specialists Conference, 2008*, pp. 1243–1249.

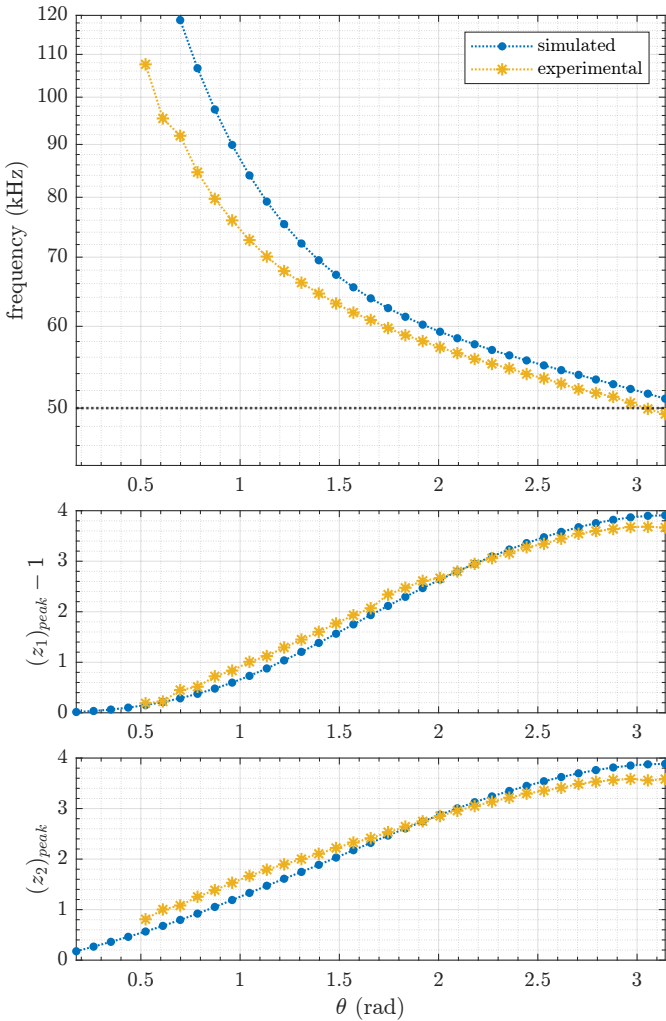


Fig. 11. Comparison between the experiments and the simulations with $R = 10.1 \Omega$. The black dotted line corresponds to the estimated resonant frequency $f_0 = 50$ kHz.

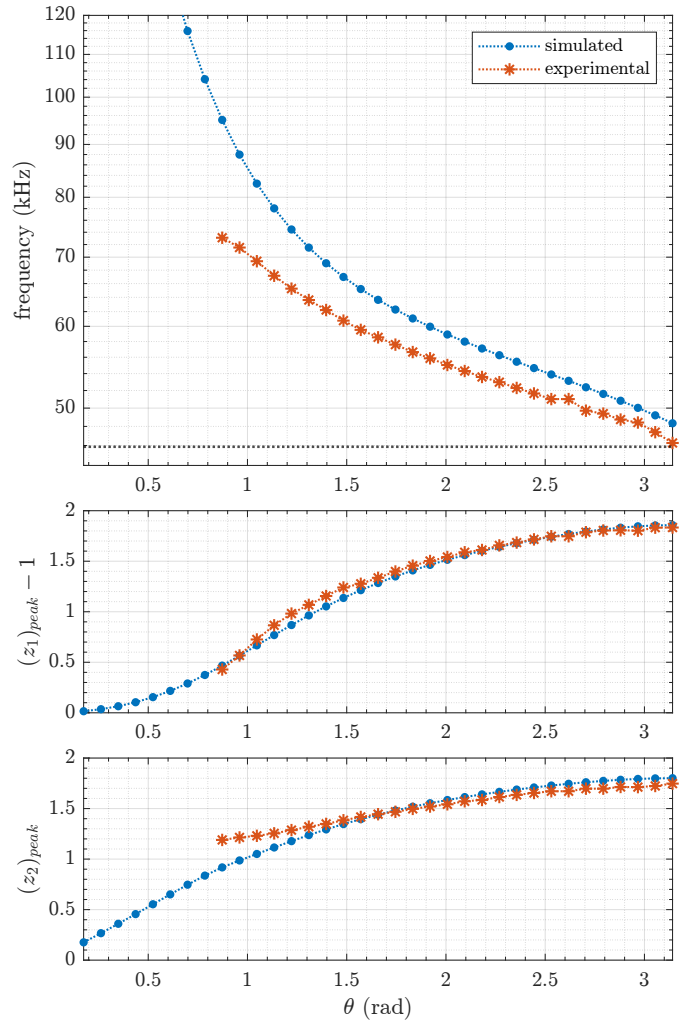


Fig. 12. Comparison between the experiments and the simulations with $R = 22 \Omega$. The black dotted line corresponds to the estimated resonant frequency $f_0 = 45.8$ kHz.